

Constraining Models of New Physics in Light of Recent Experimental Results on $a_{\psi K_S}$

Sven Bergmann and Gilad Perez

Department of Particle Physics, Weizmann Institute of Science, Rehovot 76100, Israel

Abstract

We study extensions of the Standard Model where the charged current weak interactions are governed by the CKM matrix and where all tree-level decays are dominated by their Standard Model contribution. We constrain both analytically and numerically the ratio and the phase difference between the New Physics and the Standard Model contributions to the mixing amplitude of the neutral B system using the experimental results on R_u , $\Delta m_{d,s}$, ε_K and $a_{\psi K_S}$. We present new results concerning models with minimal flavor violation and update the relevant parameter space. We also study the left-right symmetric model with spontaneously broken CP, probing the viability of this model in view of the recent results for $a_{\psi K_S}$ and other observables.

I. INTRODUCTION

For more than 30 years the only unambiguous indication for CP violation (CPV) was found in the neutral kaon system. Even though the CP violating parameter

$$\varepsilon_K = (2.280 \pm 0.013) \times 10^{-3} e^{i\phi_\varepsilon} \quad \text{with} \quad \phi_\varepsilon \simeq \pi/4 \quad (1)$$

has been measured rather accurately [1], hadronic uncertainties obscure the determination of the fundamental CKM parameters [2]. However, there is growing evidence that CPV also occurs in the B meson system. Specifically, indications for a CP asymmetry in $B_d \rightarrow J/\psi K_S$ decays have been reported by the ALEPH [3], BaBar [4], BELLE [5], CDF [6] and OPAL [7] collaborations. Combining all the measurement gives:

$$a_{\psi K_S} = 0.51 \pm 0.18. \quad (2)$$

It is essential to understand the impact of the present and upcoming experimental data on the SM and its extensions. In this paper we focus on a large class of NP models where the charged current weak interactions are governed by a 3×3 unitary matrix, just like in the CKM picture. Moreover, we make the reasonable assumption that all tree-level decays are dominated by their SM contribution. However, flavor changing neutral current processes are sensitive to New Physics (NP) because, in the SM, they appear only at the loop level.

After a brief update on the SM picture, we study in detail, both analytically and numerically, the allowed parameter space of the ratio and the phase difference between the NP and the SM contributions to the mixing amplitude of the neutral B system. We use the experimental results on R_u , $\Delta m_{d,s}$, ε_K and $a_{\psi K_S}$ for the generic NP models. Besides the two general assumptions mentioned above we introduce additional constraints that apply to specific NP models. First, we assume that the ratio between the mass differences of the B_d and the B_s neutral meson system is unaffected by NP, which is valid, *e.g.*, in models with Minimal Flavor Violation (MFV). Second, we impose a small CP violating phase, as for example in left-right symmetric (LRS) models with spontaneous CPV.

We devote special attention to models of MFV. We show that the three parameters ρ , η and F_{tt} can be obtained analytically from the experimental results on R_u , Δm_d and ε_K . Additional constraints on the parameter space arise from the measurement of $a_{\psi K_S}$ and the upper bound on $\Delta m_d/\Delta m_s$.

Finally, we investigate the impact of the uncertainty of various parameters in LRS models with spontaneous CPV on recent claims that these models would be ruled out by a significant CP asymmetry in $B_d \rightarrow J/\psi K_S$ decays.

II. STANDARD MODEL PICTURE

CPV appears naturally in the Standard Model with three generations of quarks. It can be attributed to a single phase, δ_{KM} , appearing in the CKM matrix that describes the weak charged-current interactions. Among the four Wolfenstein parameters (λ, A, ρ, η) that provide a convenient description of the CKM matrix [8] only two have been determined with a good accuracy [1], namely

$$\lambda = 0.2237 \pm 0.0033 \quad \text{and} \quad A = 0.819 \pm 0.040. \quad (3)$$

The other two parameters (ρ, η) describing the apex of the *unitarity triangle*, that follows from the unitarity relation $V_{ud}V_{ub}^* + V_{cd}V_{cb}^* + V_{td}V_{tb}^* = 0$, have a rather large uncertainty. As a consequence the CP violating phase $\delta_{KM} = \arctan(\eta/\rho)$ of the SM is relatively weakly constrained.

In the following we review briefly how the allowed region for the two Wolfenstein parameters ρ and η is obtained (for more details see *e.g.* [9,10] and references therein). At

present these parameters are experimentally constrained by the measurement of $|V_{ub}/V_{cb}|$, the observed $B_d^0 - \bar{B}_d^0$ mixing parameter Δm_d , the lower bound on the $B_s^0 - \bar{B}_s^0$ mixing parameter Δm_s , the measurement of ε_K and the combined result for $a_{\psi K_S}$. Note that for the purpose of this paper it is sufficient to work to leading order in λ^2 and we therefore neglect all subdominant contributions.

The distance from the origin to the apex (ρ, η) of the rescaled unitarity triangle,

$$\sqrt{\rho^2 + \eta^2} \simeq R_u \equiv \left| \frac{V_{ub}^* V_{ud}}{V_{cb}^* V_{cd}} \right|, \quad (4)$$

is proportional to $|V_{ub}/V_{cb}|$, which dominates its uncertainty. The ratio $|V_{ub}/V_{cb}|$ can be determined from various tree-level B decays (see *e.g.* [11] and Tab 1.), restricting R_u to the interval

$$R_u \in [0.34, 0.43]. \quad (5)$$

The distance between the apex of the rescaled unitarity triangle and the point $(1, 0)$ in the $\rho - \eta$ plane is given by:

$$\sqrt{(\rho - 1)^2 + \eta^2} \simeq R_t \equiv \left| \frac{V_{tb}^* V_{td}}{V_{cb}^* V_{cd}} \right|. \quad (6)$$

R_t can be determined from the experimental results for mass differences Δm_q in the $B_q^0 - \bar{B}_q^0$ ($q = d, s$) systems by means of the SM predictions (see *e.g.* [9,10]):

$$\Delta m_q = \frac{G_F^2}{6\pi^2} \eta_B m_{B_q} m_W^2 f_{B_q}^2 B_{B_q} S_0(x_t) \cdot |V_{tq} V_{tb}^*|^2. \quad (7)$$

Here G_F is the Fermi constant, η_B is a QCD correction factor, m_{B_q} is the B_q^0 mass, m_W is the W -boson mass, f_{B_q} is the B_q decay constant, B_{B_q} parameterizes the value of the relevant hadronic matrix element and $S_0(x_t)$ gives the electroweak loop contribution as a function of the top quark mass $m_t^2 = x_t m_W^2$. Also the ratio $\Delta m_d/\Delta m_s$ is very useful since it is simply related to R_t via

$$\frac{\Delta m_d}{\Delta m_s} \simeq R_t^2 \frac{\lambda^2}{\xi^2} \cdot \frac{m_{B_d}}{m_{B_s}}, \quad (8)$$

where $\xi \equiv f_{B_s}/f_{B_d} \cdot \sqrt{B_{B_s}/B_{B_d}}$.

The measurement of the ε_K parameter in combination with the SM prediction determines a region between two hyperbolae in the $\rho - \eta$ plane, described by (see *e.g.* [9,10]):

$$\eta \left[(1 - \rho) \eta_2 S_0(x_t) A^2 + P_c \right] A^2 B_K \simeq 0.226. \quad (9)$$

Here η_2 is a QCD correction factor and P_c characterizes the contributions with one or two intermediate charm-quarks.

Finally the recent results for the CP asymmetry in the $B_d^0 \rightarrow J/\psi K_S$ decay in eq. (2) imply a further constraint in the $\rho - \eta$ plane via the SM prediction

$$a_{\psi K_S} = \sin 2\beta, \quad (10)$$

where

$$\beta \equiv \arg \left(-\frac{V_{cd}V_{cb}^*}{V_{td}V_{tb}^*} \right). \quad (11)$$

In terms of the Wolfenstein parameters we have

$$\sin 2\beta \simeq \frac{2\eta(1-\rho)}{\eta^2 + (1-\rho)^2}. \quad (12)$$

Combining the above formulae and using the input parameters in Tab. 1 we obtain the allowed region for (ρ, η) shown in Fig. 1. Note that we naively combine the aforementioned constraints in order to determine the allowed region. (For more sophisticated analyses see *e.g.* refs. [12,13,11,14].)

III. GENERIC NEW PHYSICS MODELS WITH UNITARY MIXING MATRIX

We focus our analysis on a large class of new physics (NP) models with the following two features (c.f. refs [15–17] and references therein):

- (i) The 3×3 mixing matrix for the charged current weak interactions is unitary.
- (ii) Tree-level decays are dominated by the SM contributions.

Note that assumption (i) holds in all SM extensions with three quark generations. Assumption (ii) implies in particular that the phase of the $B \rightarrow \psi K_S$ decay amplitude is given by the Standard Model CKM phase, $\arg(V_{cb}V_{cs}^*)$. Both assumptions are satisfied by a wide class of models, like supersymmetry with R -parity, various LRS models, models with minimal flavor violation (MFV) and several multi-Higgs models. Since some of the models mentioned above have additional features we investigate the following three scenarios:

- (a) *Only* assumptions (i) and (ii) are valid.
- (b) Assumptions (i) and (ii) apply *and* $\Delta m_d/\Delta m_s$ is unaffected by the presence of NP.
- (c) Assumptions (i) and (ii) apply *and* δ_{KM} is small.

Scenario (b) contains, for example, certain multi-Higgs models with “flavor conservation” and models with MFV [10,18–20]. Scenario (c) applies to models of approximate CP symmetry and LRS models with spontaneous CPV [21–28]. To be specific we take $|\tan(\delta_{KM})| < \tan(\delta^{max}) = 0.25$ for these scenarios.

The NP effects relevant to our analysis modify the $B_d-\bar{B}_d$ mixing amplitude, $M_{12}-\frac{i}{2}\Gamma_{12}$. Assumption (ii) implies that the impact of NP on the absorptive part of this amplitude is negligible:

$$\Gamma_{12} \approx \Gamma_{12}^{\text{SM}}. \quad (13)$$

The modification of M_{12} can be parameterized as follows (see refs. [15,16,29] and refs. therein):

$$\frac{M_{12}}{M_{12}^{\text{SM}}} = r_d^2 e^{2i\theta_d}. \quad (14)$$

The variables r_d and θ_d relate directly to the experimental observables. The results for $\Delta m_{d,s}$ constrain r_d^2 , while the recent measurement of $a_{\psi K_S}$ restricts the value of the phase $2\theta_d$. However, to investigate a specific model it is convenient to use different variables, h and σ , and describe the NP modifications to the amplitude $M_{12} = M_{12}^{\text{SM}} + M_{12}^{\text{NP}}$ via [15,16,29]:

$$\frac{M_{12}^{\text{NP}}}{M_{12}^{\text{SM}}} = h e^{i\sigma}. \quad (15)$$

The variables h and σ are related to r_d and θ_d through:

$$r_d^2 e^{2i\theta_d} = 1 + h e^{i\sigma}. \quad (16)$$

Our goal is to determine the allowed parameter space for h and σ . To this end we first constrain r_d^2 and $2\theta_d$ using the relevant experimental results on R_u , $\Delta m_{d,s}$, ε_K and $a_{\psi K_S}$. Then we show how to translate the ranges for r_d^2 and $2\theta_d$ into the allowed region in the $h-\sigma$ plane. All the relevant parameters we use in our analysis are summarized in Tab. 1. For most of these parameters we adopt the values of ref. [11]. For simplicity we scan over the ranges indicated in Tab. 1 both for the theoretical and experimental parameters.

A. Constraining r_d and θ_d

The parameter r_d^2 is constrained by the results for $\Delta m_{d,s}$ [15,16]. In models that satisfy the assumptions (i) and (ii) the expressions for $\Delta m_{d,s}$ in eq. (7) have to be modified as follows [15]:

$$\Delta m_q = \frac{G_F^2}{6\pi^2} \eta_B m_{B_q} m_W^2 f_{B_q}^2 B_{B_q} S_0(x_t) |V_{tq} V_{tb}^*|^2 \cdot r_q^2, \quad (17)$$

where $q = d, s$ and r_s is the analog to r_d for the B_s system. Moreover $\Delta m_{B_d}/\Delta m_{B_s}$ satisfies:

$$\frac{\Delta m_{B_d}}{\Delta m_{B_s}} \simeq \lambda^2 R_t^2 \cdot \xi^{-2} \frac{m_{B_d}}{m_{B_s}} \left(\frac{r_d}{r_s} \right)^2, \quad (18)$$

which reduces to the SM expression in eq. (8) when $r_d = r_s$. Note, that the constraint on R_u given in eq. (4) is unchanged by NP, since it is dominated by tree-level amplitudes.

Using the values in Tab. 1, from eq. (17) it follows that:

$$0.69 < r_d \cdot R_t(\rho, \eta) < 1.03, \quad (19)$$

while eq. (18) implies that

$$\frac{r_d}{r_s} R_t(\rho, \eta) \leq 0.99. \quad (20)$$

The allowed range for the phase θ_d is restricted by the measurement of $a_{\psi K_S}$ [15]. Due to the two-fold ambiguity of the sin function, the one-sigma result for $a_{\psi K_S}$ in eq. (2) corresponds to two allowed intervals for $2(\theta_d + \beta)$ [15,16]:

$$19^\circ \lesssim 2(\theta_d + \beta) \lesssim 44^\circ \quad \text{or} \quad 19^\circ \lesssim 180^\circ - 2(\theta_d + \beta) \lesssim 44^\circ. \quad (21)$$

We use the above results for two types of analysis: In our numerical analysis we scan over the $\rho - \eta$ plane and calculate the allowed intervals for r_d according to eq. (19) [and eq. (20) in scenario (b)] and θ_d from eq. (21) for all points (ρ, η) that fulfill the constraints relevant to a particular scenario (c.f. Fig. 2 for scenario (a), Fig. 4 for scenario (b) and Fig. 6 for scenario (c), respectively).

To get better insight into the numerical results we have performed an analytical calculation, where we use the maximal allowed region for r_d and θ_d that follow from the *global* constraints on R_t and β . Such an approach is particularly useful, because the analytical constraints can easily be updated using the forthcoming experimental data. Moreover the system of constraints may be extended for different classes of NP models. For scenario (a) we get (see appendix A 1 for details):

$$r_d \in [0.5, 1.8] \quad \text{and} \quad 2\theta_d \in [-32^\circ, 212^\circ]. \quad (22)$$

Note that the interval for $2\theta_d$ in eq. (22) is independent of the upper bound on $a_{\psi K_S}$ as long as $(2\theta_d)_{max_1} > (2\theta_d)^{min_2}$. With the upper bound on R_u in eq. (4) two distinct intervals for $2\theta_d$ only appear if $(a_{\psi K_S})_{max} < 0.63$. This explains why the global constraint on $2\theta_d$ we obtain from the measurement of $a_{\psi K_S}$ in eq. (2) almost coincides with the one in ref. [15], even though our upper bound on $a_{\psi K_S}$ is much more stringent.

For scenario (b) the lower bound on r_d is somewhat stronger, since from eq. (20) it follows that $R_t(\rho, \eta) \leq 0.99$, which gives $r_d > 0.7$. In scenario (c) we have

$$r_d \in [0.5, 0.8] \quad \text{with} \quad 2\theta_d \in [12^\circ, 51^\circ] \cup [129^\circ, 168^\circ], \quad (23)$$

for the allowed regions with $\rho < 0$ and

$$r_d \in [1.0, 1.8] \quad \text{with} \quad 2\theta_d \in [-1^\circ, 64^\circ] \cup [116^\circ, 181^\circ], \quad (24)$$

for the allowed regions with $\rho > 0$ (c.f. Fig. 6).

B. Constraining h and σ

Our first observation is that from the maximal value for r_d one obtains an upper bound on h . Eq. (16) implies that

$$h(r_d, \theta_d) = \sqrt{r_d^4 - 2r_d^2 \cos 2\theta_d + 1} \leq (r_d^{max})^2 + 1 \approx 4.24, \quad (25)$$

where the upper bound arises from setting $\cos 2\theta_d = -1$ and $r_d = r_d^{max}$. Still, one can obtain much better bounds using the correlation between h and σ . Here we only sketch how to translate the constraints one obtains for r_d^2 and $2\theta_d$ into those for h and σ . The details can be found in appendix A 2. The basic idea is simple. We solve eq. (16) for h , once eliminating θ_d ,

$$h^\pm(\sigma, r_d) \equiv -\cos \sigma \pm \sqrt{\cos^2 \sigma + r_d^4 - 1}, \quad (26)$$

and once eliminating r_d ,

$$h^\pm(\sigma, \theta_d) = \frac{\sin 2\theta_d \sin(2\theta_d \pm \sigma)}{\sin^2 \sigma - \sin^2 2\theta_d}. \quad (27)$$

Using the above equations the ranges for r_d and θ_d can be translated into a region in the $h - \sigma$ plane. The overlap of the two areas from eq. (26) and eq. (27) corresponds to the allowed region in the $h - \sigma$ parameter space. While this method is straightforward one has to treat carefully the discrete ambiguities of the trigonometric functions (see appendix).

Using eq. (26) and eq. (27) the global constraints on r_d and θ_d in eqs. (22)–(24) can be readily translated into the allowed region for h and σ . Combining all the resulting intervals one obtains the light areas, whose boundaries are given by $h^\pm(\sigma, r_d)$ and $h^\pm(\sigma, \theta_d)$ with r_d and θ_d at the edges of their allowed intervals (see appendix A 2 for more details).

In order to obtain the exact allowed region in the $h - \sigma$ plane we have performed a numerical analysis proceeding as follows: Rather than using the global constraints on r_d and θ_d corresponding to the entire allowed region in the $\rho - \eta$ plane, we compute the possible ranges for r_d and θ_d for *each* permissible value of ρ and η . That is we scan over the $\rho - \eta$ plane and for all points (ρ, η) that fulfill the constraints relevant to a particular scenario, we calculate the allowed intervals for r_d according to eq. (19) [and eq. (20) in scenario (b)]

and θ_d from eq. (21). The resulting intervals are then translated into the corresponding region in the $h - \sigma$ plane, just as we did in the “global” analysis, but for each point (ρ, η) separately. Combining all the resulting intervals one obtains the allowed regions indicated as the dark areas in Fig. 3, Fig. 5 and Fig. 7. They are contained within the light areas resulting from the analytic boundaries from the global constraints. Even though in general the numerical results are not much more constraining than the global ones, there exist some regions where the numerical constraints are significantly stronger than the analytical boundaries. For example, there appear “holes” in the dark gray regions of Fig. 3 and Fig. 5 that correspond to the excluded region within the R_u annulus, which has been ignored in “global” analysis (light gray regions). Even more important, the lower bound on h in scenario (c) (see Fig. 7) from the numerical analysis turns out to be significantly stronger than in the global analysis, which is marginally consistent with $h = 0$.

C. Summary of Results

- (a) Generic models: All models that satisfy the assumptions (i) and (ii) must respect the condition in eq. (4), which corresponds to an annulus around the origin in the $\rho - \eta$ plane as shown in Fig. 2. The resulting allowed region in the $h - \sigma$ plane is presented in Fig. 3. The admissible range for h is given by:

$$h \in [0, 4.2]. \quad (28)$$

- (b) Models where $\Delta m_d^{SM}/\Delta m_s^{SM} \approx \Delta m_d/\Delta m_s$: The relevant region in the $\rho - \eta$ plane is shown in Fig. 4 and the resulting allowed region in the $h - \sigma$ plane is presented in Fig. 5. The admissible range for h is the same as in eq. (28), but the excluded area in the $h - \sigma$ plane is somewhat larger.

- (c) Models in which δ^{KM} is significantly smaller than unity: The relevant region in the $\rho - \eta$ plane for this class of models is shown in Fig. 6 and the resulting allowed region in the $h - \sigma$ plane is presented in Fig. 7. The excluded region is significantly smaller than in scenario (a) and (b). The admissible range for h and σ are given by:

$$h \in [0.14, 4.18] \quad \text{and} \quad \sigma \in [0^\circ, 180^\circ]. \quad (29)$$

Unlike for scenarios (a) and (b) in this case h has also a non-trivial lower bound and σ has an upper bound. Consequently NP contributions to the $B - \bar{B}$ mixing amplitude are required in this scenario.

IV. SPECIFIC NEW PHYSICS MODELS

In this section we focus on two specific New Physics models that belong to the general class of models discussed above. We discuss first models with minimal flavor violation (MFV) and subsequently we present some new results relevant to LRS models with spontaneous CPV.

A. Minimal Flavor Violation

Models with MFV comprise the SM and those extensions of the SM in which all flavor changing interactions are described by the CKM matrix. These models do not introduce any new operators implying the absence of any new CP violating phases beyond the KM phase. The only impact of MFV models are modifications of the Wilson coefficients of the SM operators due to additional contributions from diagrams involving new internal particles [10,18–20].

1. Constraints from R_u , $\Delta m_{d,s}$ and ε_K

In the framework of this analysis the only relevant modifications of the SM predictions concern the mass difference Δm_d of the B_d system and the parameter ε_K describing CP violation in $K^0 - \bar{K}^0$ mixing. It turns out that for both parameters the new physics charm and charm-top contributions are negligible and that additional contributions to the SM box diagram with top quark exchanges can be described by one single parameter F_{tt} .

This parameter effectively replaces the relevant Inami-Lim function $S_0(x_t)$ appearing in eqs. (7) and (9), which have to be substituted by [18]

$$\Delta m_d = \frac{G_F^2}{6\pi^2} \eta_B m_{B_d} m_W^2 f_{B_d}^2 B_{B_d} F_{tt} \cdot |V_{td} V_{tb}^*|^2. \quad (30)$$

and

$$\eta \left[(1 - \rho) \eta_2 F_{tt} A^2 + P_c \right] A^2 B_K \simeq 0.226, \quad (31)$$

respectively. The constraint on the unitarity triangle from R_u [c.f. eq. (4)] remains unaffected in MFV models, because it is dominated by tree-level contributions. Furthermore, due to the absence of any new phases in the $B - \bar{B}$ mixing amplitude the SM prediction for $a_{\psi K_S}$ [c.f. eqs. (10)-(12)] is unchanged. Finally, $\Delta m_d / \Delta m_s$ in eq. (8) remains unaffected since the NP contributions cancel each other in the ratio.

The important point we want to make is that for any given set of the parameters R_u, A, B_K, P_c and

$$\Delta_f \equiv \frac{\Delta m_d}{B_{B_d} f_B^2 \lambda^6} \quad (32)$$

one can obtain exact expressions for ρ , η and F_{tt} . Combining eqs. (4), (30) and (31) results into a quartic equation that can be solved analytically. For example, for ρ one obtains

$$(R_u^2 - \rho^2) \left[(1 - \rho) C_\Delta + C_c (1 - 2\rho + R_u^2) \right]^2 = \left[C_\varepsilon (1 - 2\rho + R_u^2) \right]^2, \quad (33)$$

where

$$C_\Delta \equiv \frac{6\pi^2 \Delta_f}{G_F^2 \eta_B m_{B_d} M_W^2 A^2}, \quad C_\varepsilon \equiv \frac{0.226}{A^4 B_K \eta_2}, \quad \text{and} \quad C_c \equiv \frac{P_c}{A^2 \eta_2}. \quad (34)$$

We have used the analytic expressions to obtain the allowed regions for ρ , η and F_{tt} by scanning over the intervals for R_u , A , B_K , P_c and Δ_f in Tab. 2. *A priori* up to four solutions are possible, but for the present ranges of the parameters R_u , A , B_K , P_c and Δ_f only two solutions are real (see Fig. 8 and Fig. 9). Adding the constraint from $\Delta m_d / \Delta m_s$ in eq. (8) practically the entire solution shown in Fig. 8 is ruled out and only the second solution in Fig. 9 remains viable. We find that F_{tt} is restricted to the interval

$$F_{tt} \in [1.2, 5.7], \quad (35)$$

which includes the SM value $F_{tt}^{SM} \equiv S_0(x_t) \simeq 2.46 (m_t / 170 \text{ GeV})^{1.52}$ [10].

The value of $\sin 2\beta$ within models of MFV has obtained considerable attention recently [30,10,12]. In particular it was shown in ref. [30] that there exists a lower bound on $\sin 2\beta$ in these models. The existence of this bound is a non-trivial result of the correlation between Δm_d and ε_K which holds in models of MFV [30]. Using the analytic solutions for ρ , η and F_{tt} we have investigated the behavior of $\sin 2\beta$ as a function of R_u , A , B_K , P_c and Δ_f . We find that it takes its minimal value, $(\sin 2\beta)_{min}$, when R_u is minimal and all the other parameters are maximal. While the size of the exact expressions we obtained for ρ , η , F_{tt} and $\sin 2\beta$ preclude its presentation here, one can use the results to expand these parameters around a particular value. For example a linear expansion of $\sin 2\beta$ around R_u^{min} , A^{max} , B_K^{max} , P_c^{max} and Δ_f^{max} gives:

$$\begin{aligned} \sin 2\beta \simeq & 0.52 + 0.23 (R_u - 0.34) - 1.09 (A - 0.86) - 0.47 (B_K - 1.00) \\ & - 0.31 (P_c - 0.36) - 3.43 \times 10^{-6} \left(\frac{\Delta_f}{\text{ps}^{-1} \text{ GeV}^{-2}} - 1.04 \times 10^5 \right). \end{aligned} \quad (36)$$

This expansion provides a good approximation to the exact expression for $\sin 2\beta$ within most of the allowed parameter space for R_u , A , B_K , P_c and Δ_f . Moreover we find that for reasonable changes in the boundaries of the respective intervals, $\sin 2\beta$ remains minimal when R_u is minimal and all the other parameters are maximal. Thus one can use eq. (36) to recalculate $(\sin 2\beta)_{min}$ for somewhat different values of R_u^{min} , A^{max} , B_K^{max} , P_c^{max} and Δ_f^{max} .

For example using the more conservative values of ref. [10] one recovers the corresponding lower bound on $\sin 2\beta$ which is somewhat weaker than our result,

$$(\sin 2\beta)_{min} = 0.52. \quad (37)$$

We note that the upper bound on $\sin 2\beta$,

$$(\sin 2\beta)_{max} = 2R_u^{max} \sqrt{1 - (R_u^{max})^2} = 0.78, \quad (38)$$

is determined by the tangent to the R_u annulus as in the SM [31].

Conversely, the range of $\sin 2\beta$ due to the measured value of $a_{\psi K_S}$ restricts the parameter F_{tt} . Remarkably, taking the one-sigma range in eq. (2), only the lower bound on F_{tt} is slightly improved to $F_{tt}^{min} = 1.3$. The reason is evident from Fig. 9: Even though the upper bound on $\sin 2\beta$ removes a substantial part of the allowed region, the remaining solution (below the upper gray line) still extends over a wide range for the parameter F_{tt} (as indicated by the gray-scale).

Finally we note that the allowed interval for F_{tt} is consistent with the result obtained in the generic framework discussed in section III. Indeed the ranges for h at $\sigma = 0$ or $\sigma = \pi$ in Fig. 5 include the values for h^{MFV} defined via

$$h^{MFV} e^{i\sigma^{MFV}} \equiv (F_{tt}/F_{tt}^{SM} - 1) \in [-0.48, 1.51], \quad (39)$$

where – due to the absence of new phases in MFV models – either $\sigma^{MFV} = 0$ if $F_{tt} \geq F_{tt}^{SM}$ or $\sigma^{MFV} = \pi$ if $F_{tt} < F_{tt}^{SM}$.

To conclude, models of MFV provide a consistent explanation of all the relevant experimental data. However, due to the $\Delta m_d/\Delta m_s$ constraint the allowed region in the $\rho - \eta$ plane is similar to the one of the SM and F_{tt} is close to F_{tt}^{SM} . Therefore with the set of observables studied in this section it is very difficult, if not impossible, to distinguish MFV models beyond the SM. Therefore, we turn now briefly to a second set of observables which might help to disentangle such models from the SM.

2. Constraints from $Y \rightarrow X\nu\bar{\nu}$

Let us consider the decays $K^+ \rightarrow \pi^+\nu\bar{\nu}$ and $B \rightarrow X_s\nu\bar{\nu}$ within the MFV models. They are both related to the generalized Inami-Lim [32] function, $X_{\nu\bar{\nu}}$ [18,19]. The theoretical prediction for $K^+ \rightarrow \pi^+\nu\bar{\nu}$ is given by [10,18]:

$$\mathcal{B}_K \equiv \text{BR}(K^+ \rightarrow \pi^+\nu\bar{\nu})/\kappa_+ \approx \left\{ \left(A^2 \eta X_{\nu\bar{\nu}} \right)^2 + \left[P_0(X) + A^2(1 - \rho) X_{\nu\bar{\nu}} \right]^2 \right\}, \quad (40)$$

where the values of $P_0(X)$ and κ_+ are given in Tab. 1.

Using eq. (40) from the experimental value of $\text{BR}(K^+ \rightarrow \pi^+\nu\bar{\nu})$ (given in Tab. 1) and the value of κ_+ we get:

$$0.7 = \mathcal{B}_K^{min} < \left(A^2 X_{\nu\bar{\nu}} R_t \right)^2 + 2P_0(X) A^2 X_{\nu\bar{\nu}} (1 - \rho) + P_0(X)^2 < \mathcal{B}_K^{max} = 11.9, \quad (41)$$

where \mathcal{B}_K^{min} (\mathcal{B}_K^{max}) denotes the minimal (maximal) value of \mathcal{B}_K . From eq. (41) it follows that $X_{\nu\bar{\nu}} \in [X_+^{min}, X_+^{max}]$ or $X_{\nu\bar{\nu}} \in [X_-^{max}, X_-^{min}]$, where

$$X_{\pm}^{min} \equiv \frac{1}{A^2 R_t^2} \left[P_0(X)(\rho - 1) \pm \sqrt{R_t^2 \mathcal{B}_K^{min} - \eta^2 P_0(X)} \right], \quad (42)$$

$$X_{\pm}^{max} \equiv \frac{1}{A^2 R_t^2} \left[P_0(X)(\rho - 1) \pm \sqrt{R_t^2 \mathcal{B}_K^{max} - \eta^2 P_0(X)} \right]. \quad (43)$$

A scan of the allowed $\rho - \eta$ region in Fig. 9 (including the $a_{\psi K_S}$ constraint) and the intervals for A and $P_0(X)$ yields the following two ranges for $(X_{\nu\bar{\nu}})$:

$$0.5 < X_{\nu\bar{\nu}} < 7.8 \quad \text{or} \quad -9.8 < X_{\nu\bar{\nu}} < -1.6. \quad (44)$$

Note that the uncertainty related to the measurement of $\text{BR}(K^+ \rightarrow \pi^+ \nu\bar{\nu})$ (given in Tab. 1) is based on observation of a single event. Therefore, the ranges given in eq. (44) correspond to a confidence level of somewhat less than 67 %.

Within MFV models the decay $B \rightarrow X_s \nu\bar{\nu}$ is also related to the parameter $X_{\nu\bar{\nu}}$ [10,18]. The prediction for the branching ratio,

$$\text{BR}(B \rightarrow X_s \nu\bar{\nu}) \approx 1.5 \cdot 10^{-5} \cdot X_{\nu\bar{\nu}}^2, \quad (45)$$

in combination with the experimental bound (given in Tab. 1):

$$\text{BR}(B \rightarrow X_s \nu\bar{\nu}) < 6.4 \cdot 10^{-4}, \quad (46)$$

provides a second constraint on $X_{\nu\bar{\nu}}$:

$$|X_{\nu\bar{\nu}}| \lesssim 6.6, \quad (47)$$

which excludes some of the allowed range given in eq. (44). Combining the two ranges yields:

$$0.5 < X_{\nu\bar{\nu}} < 6.6 \quad \text{or} \quad -6.6 < X_{\nu\bar{\nu}} < -1.6. \quad (48)$$

We note that in principle also the decay $B \rightarrow X_d \nu\bar{\nu}$ could provide a constraint on $X_{\nu\bar{\nu}}$, but since it is suppressed by V_{td}/V_{ts} with respect to $B \rightarrow X_s \nu\bar{\nu}$ its branching ratio is decreased by roughly an order of magnitude and therefore at present less useful.

Currently the constraints are too weak to rule out one of the two intervals, but the forth-coming data on K and B decays with final neutrinos will eventually allow to pin down the value of $X_{\nu\bar{\nu}}$ and maybe provide evidence for MFV beyond the SM if $X_{\nu\bar{\nu}}$ turns out to be different from its SM value $X_{\nu\bar{\nu}}^{SM} = X(x_t) \approx 1.5$ [10]. In this context also the observable $(\varepsilon'/\varepsilon)_K$ could be useful, since it depends on a related parameter $X_{u\bar{u}}$, which in some models roughly agrees with $X_{\nu\bar{\nu}}$ (compare for example the values for $X_{u\bar{u}}$ and $X_{\nu\bar{\nu}}$ in ref. [19]).

B. LRS Model with Spontaneous CP Violation

The spontaneously broken LRS (SBLR) model has been studied in detail in refs. [21–28] (see also references therein). Here we focus on the impact of the measurement of $a_{\psi K_S}$ in eq. (2) on this model. The important feature of the SBLR model is that essentially all the phases and therefore the CPV observables depend on one parameter. In a certain phase convention [22–25] this parameter is written as $r \sin \alpha$ with $|r| \lesssim m_b/m_t$ (see also refs. [21,27]). Due to this single parameter the model is very predictive.

The problem is that part of the model has not yet been solved analytically. In particular analytic expressions for the phases of the left and right CKM-like mixing matrices exist only within the “small phase approximation” [21–25], which is valid for $r \sin \alpha \lesssim 0.01$. Nevertheless a very thorough numerical analysis, beyond the small phase approximation, has been performed by Ball *et. al.* in ref. [27], calculating the predictions for several CPV observables and discussing the limitation of the small phase approximation. In particular it was found that within the LRSB model the measurement of ε_K in eq. (1) and other observables implies

$$(a_{\psi K_S})_{LRSB} \lesssim 0.1, \quad (49)$$

which is inconsistent with the combined measurement in eq. (2). It is important to note, however, that the analysis in ref. [27] only used the central values for various input parameters which are subject to theoretical and experimental uncertainties. Therefore we find it timely to reinvestigate the prediction in eq. (49) including these uncertainties and using the most recent values for the central values.

1. The Analysis

We restrict our analysis to the regime in which the small phase approximation is valid, which allows us to use the analytic expression for various observables of the K and B system.

We scan over the entire parameter space of the relevant input parameters according to their uncertainties in order to find the subspace consistent with all the measured observables. In particular, we test all the 32 different sign combinations of the quark masses, and allow the CKM phase δ to be centered both around 0 and π (c.f. discussion in ref. [33]) which yields altogether 64 different signatures. For each permissible subspace we calculate the corresponding predicted range for $a_{\psi K_S}$.

Most of the analytic expression in the small phase approximation have been calculated in refs. [22–24]. For notations and phase conventions we refer the reader to refs. [23,24]. (Note that the parametrization of CKM matrix used in ref. [22] is the Kobayashi-Maskawa convention [2] and not the Chau-Keung convention [34], which is commonly used.) All the parameters relevant to our analysis can be found in Tab. 2.

For the kaon system we consider the observables Δm_K , ε_K and $(\varepsilon'/\varepsilon)_K$. The effective Lagrangian $\mathcal{L}^{\Delta S=2}$, that describes the $\Delta S = 2$ processes, is given in eq. (19) of ref. [23]. The relevant phases of the left and right mixing matrices, δ_1 , δ_2 , γ and δ have been calculated in ref. [22]. We use the following three constraints:

- (i) Δm_K : Due to the lack of reliable predictions for the long distance contributions we require that the short distance contribution should at most saturate Δm_K , i.e.

$$2|M_{12}^K| < \Delta m_K^{\text{exp}}, \quad (50)$$

where $M_{12}^K = \langle K^0 | \mathcal{L}^{\Delta S=2} | \bar{K}^0 \rangle / (2m_K)$.

- (ii) ε_K : We use the upper and lower bound given in ref. [27]:

$$6.375 \cdot 10^{-3} - 0.01 \cdot \left(\frac{1 \text{ TeV}}{M_2} \right)^2 < \tilde{\theta}_M < 6.523 \cdot 10^{-3} + 0.01 \cdot \left(\frac{1 \text{ TeV}}{M_2} \right)^2, \quad (51)$$

where, in our case, $\tilde{\theta}_M \approx \left| \frac{2 \text{Re} M_{12}}{\Delta m_K} \right| \sin(\arg M_{12})$.

- (iii) $\mathcal{R}e(\varepsilon'/\varepsilon)_K$: Due to the large hadronic uncertainties in the calculation of ε'_K we only demand that the sign predicted by the SBLR model is positive in order to be consistent [27] with recent measurements [35]. Thus, for the computation of $\mathcal{R}e(\varepsilon'/\varepsilon)_K$ it is sufficient to use the rough approximation given in eqs. (27) and (28) of ref. [22].

For the B system we consider Δm_q ($q = d, s$) and $a_{\psi K_S}$. The value of $h_q^{\text{LR}} \equiv \frac{M_{12}^{q \text{ LR}}}{M_{12}^{q \text{ SM}}}$, where $M_{12}^q = \langle B_q^0 | \mathcal{L}^{\Delta b=2} | \bar{B}_q^0 \rangle / (2m_q)$, has been calculated in ref. [27]:

$$h_q^{\text{LR}} \approx h^{\text{LR}} \equiv \frac{B_B^S(m_b)}{B_B(m_b)} \left[1.7 \left(0.051 + 0.26 \ln \frac{M_2}{1.6 \text{ TeV}} \right) \left(\frac{1.6 \text{ TeV}}{M_2} \right)^2 + \left(\frac{7 \text{ TeV}}{M_H} \right)^2 \right]. \quad (52)$$

For σ_q^{LR} an exact expression as a function of the fundamental parameters does not exist, so we use the small phase approximations [24]:

$$\sin \sigma_d^{\text{LR}} \approx \eta_d \eta_b r \sin \alpha \left[\left(\frac{\sin^2 t_1}{\eta_d m_d} + \frac{2}{\eta_s m_s} \right) \eta_c m_c + \frac{\eta_t m_t}{\eta_c m_c} \right], \quad (53)$$

$$\sin \sigma_s^{\text{LR}} \approx \eta_s \eta_b r \sin \alpha \left(\frac{\eta_c m_c}{\eta_s m_s} + \frac{\eta_t m_t}{\eta_b m_b} \right), \quad (54)$$

where t_1 , t_2 and t_3 denote the three angles of the CKM matrix in the Chau-Keung convention [34] and $\eta_i = \pm 1$ parameterizes the sign associated with the quark mass m_i . For our analysis we use the following three constraints:

(i) Δm_d : Eq. (19), eq. (52) and eq. (53) yield the constraint:

$$0.48 < \left| (V_{tb}^L V_{td}^{L*})^2 (1 + h^{LR} e^{i\sigma_d^{LR}}) \right| < 1.05, \quad (55)$$

where V_{ij}^L is the mixing matrix of the left handed current of the weak interaction.

(ii) $\frac{\Delta m_d}{\Delta m_s}$: Eq. (20), eq. (52), eq. (53), and eq. (54) yield the constraint:

$$\left| \frac{(V_{td}^{L*})^2 (1 + h^{LR} e^{i\sigma_d^{LR}})}{(V_{ts}^{L*})^2 (1 + h^{LR} e^{i\sigma_s^{LR}})} \right| < 0.98. \quad (56)$$

(iii) $a_{\psi K_S}$: In the SBLR model $a_{\psi K_S}$ is given by [27]:

$$a_{\psi K_S} \simeq \sin \left[2\beta_{\text{CKM}} + \arg \left(1 + h^{LR} e^{i\sigma_d^{LR}} \right) \right], \quad (57)$$

where

$$\beta_{\text{CKM}} \equiv \arg \left(-\frac{V_{cd}^L V_{cb}^{L*}}{V_{td}^L V_{tb}^{L*}} \right). \quad (58)$$

We require that $a_{\psi K_S}$ is positive.

2. Results

We find positive values for $a_{\psi K_S}$ that are consistent with all the experimental constraints for several signatures. The allowed range for $a_{\psi K_S}$ that results from scanning over the allowed ranges of the relevant parameters in Tab. 2 is:

$$a_{\psi K_S} \in [0, 0.3]. \quad (59)$$

In general, large values for $a_{\psi K_S}$ occur for large values of $r \sin \alpha$ for which the small phase approximation is less reliable. Still, even for the rather large values of $r \sin \alpha$ one still obtains a rough estimate for the true value of $a_{\psi K_S}$. Therefore the fact that the range given in eq. (59) is marginally consistent with the world average of $a_{\psi K_S}$ in eq. (2) gives strong indication that the inclusion of the uncertainties of the relevant parameters relaxes the upper bound on $a_{\psi K_S}$ in eq. (49) enough to make an exclusion of the LRSB model premature at this stage.

V. CONCLUSIONS

The CKM picture of the Standard Model (SM) is currently being tested with unprecedented accuracy in various experiments. In particular the B factories BELLE and BaBar provide highly interesting results. There is great hope that those or future experiments will reveal inconsistencies that indicate contributions to flavor physics from New Physics.

In this paper we have studied extensions of the Standard Model where the charged current weak interactions are governed by the CKM matrix and where all tree-level decays are dominated by the Standard Model contributions. We have constrained both analytically and numerically the ratio h and the phase difference σ between the New Physics and the Standard Model contributions to the mixing amplitude of the neutral B system using the experimental results on R_u , $\Delta m_{d,s}$, ε_K and $a_{\psi K_S}$. For generic models we find that $h < 4.2$ and the allowed region in the $h - \sigma$ plane shown in Fig. 3. Models where the ratio $\Delta m_d/\Delta m_s$ takes the Standard Model value are only slightly more constrained than the most general scenario of our framework (see Fig. 5). However imposing a small CP violating phase significantly reduces the allowed parameter space for h ($h \in [0.14, 4.18]$) and σ ($\sigma \in [0^\circ, 180^\circ]$), see Fig. 7, which requires NP contributions to the $B - \bar{B}$ mixing amplitude.

We have presented some new results for models with minimal flavor violation, pointing out that the three parameters ρ , η and F_{tt} can be obtained analytically from the experimental results on R_u , Δm_d and ε_K for any given set of rather well-determined parameters. Using the exact expressions we have updated the allowed interval of F_{tt} ($F_{tt} \in [1.3, 5.7]$) as well as $\sin 2\beta$ ($\sin 2\beta \in [0.52, 0.78]$) [for which we provide an expansion in terms of those parameters in eq. (36)]. Taking into account the analytical relation between ρ , η and F_{tt} as well as the constraints from $a_{\psi K_S}$ and $\Delta m_d/\Delta m_s$ improves significantly previous results [12].

We also consider the spontaneously broken left-right symmetric model and perform a numerical analysis using the “small phase approximation” in order to probe the viability of this model in view of the recent results for $a_{\psi K_S}$ and other observables. We find that the inclusion of the uncertainties of various input parameters relaxes the upper bound on $a_{\psi K_S}$ significantly and conclude that at present the model is still viable.

ACKNOWLEDGMENTS

We thank Y. Nir and Y. Grossman for helpful discussions and comments on the manuscript.

APPENDIX A:

1. Global constraints on r_d and θ_d

To each of the three scenarios (a), (b) and (c) corresponds a different allowed area in the $\rho - \eta$ plane (shown in Fig. 2, Fig 4 and Fig 6, respectively). Here we compute the *global* constraints on R_t and β for each scenario. From eqs. (5) and (20) it follows that in scenario (a) the allowed interval for $R_t(\rho, \eta)$ [defined in eq. (6)] is given by

$$0.57 = 1 - R_u^{max} < R_t(\rho, \eta) < 1 + R_u^{max} = 1.43. \quad (\text{A1})$$

In scenario (b) the upper bound on R_t is significantly stronger, namely $R_t < 0.99$ due to eq. (20). In scenario (c) there are two ranges, corresponding to the two allowed regions in the $\rho - \eta$ plane in Fig. 6. The upper bound on δ_{KM} implies that we have to exclude the interval

$$0.68 = \sqrt{(1 - l_\delta)^2 + h_\delta^2} < R_t(\rho, \eta) < \sqrt{(1 + l_\delta)^2 + h_\delta^2} = 1.33, \quad (\text{A2})$$

where $l_\delta \equiv R_u^{min} \cos \delta^{max}$ and $h_\delta \equiv R_u^{min} \sin \delta^{max}$, from the range in eq. (A1) in this scenario.

In scenario (a) and (b) the angle $\beta(\rho, \eta)$ [defined in eq. (11)] is restricted by the maximal value of R_u :

$$|\beta(\rho, \eta)| < \arcsin(R_u^{max}) = 25^\circ. \quad (\text{A3})$$

In scenario (c) we have

$$|\beta(\rho, \eta)| < \arctan\left(\frac{R_u^{max} \sin \delta^{max}}{1 \pm R_u^{max} \cos \delta^{max}}\right) \simeq \begin{cases} 3.5^\circ \\ 10^\circ \end{cases}, \quad (\text{A4})$$

where the plus sign refers to the region with negative ρ and the minus sign to the region with positive ρ . Using the above equations one obtains the allowed intervals for r_d and θ_d quoted in section III A in eqs. (22)–(24).

2. Analytic Boundaries in the $h - \sigma$ Plane

In this appendix we describe in detail how the allowed intervals for r_d and θ_d are translated into the allowed region in the $h - \sigma$ plane. To be specific we will use the global extrema for r_d and θ_d in section III A [c.f. eqs. (22)–(24)]. Note, however, that essentially the same equations apply for the numerical analysis, where we consider each viable point in the $\rho - \eta$ plane separately.

a. The r_d constraint

In order to obtain an equation that is independent of θ_d we take the absolute square of eq. (16):

$$r_d^2 = \sqrt{h^2 + 2h \cos \sigma + 1}. \quad (\text{A5})$$

Solving for h one has

$$h^\pm(\sigma, r_d) \equiv -\cos \sigma \pm \sqrt{\cos^2 \sigma + r_d^4 - 1}. \quad (\text{A6})$$

It follows that $h \in [h_{r_d}^{\min}, h_{r_d}^{\max}]$ where

$$h_{r_d}^{\min}(\sigma) \equiv \max(0, h^-(\sigma, r_d^{\max})) \quad \text{and} \quad h_{r_d}^{\max}(\sigma) \equiv h^+(\sigma, r_d^{\max}) \quad (\text{A7})$$

and that h is excluded from the interval $[h_{r_d}^-, h_{r_d}^+]$, where

$$h_{r_d}^-(\sigma) \equiv \max(0, h^-(\sigma, r_d^{\min})) \quad \text{and} \quad h_{r_d}^+(\sigma) \equiv h^+(\sigma, r_d^{\min}). \quad (\text{A8})$$

The function $h_{r_d}^{\max}(\sigma)$ corresponds to the upper solid curves in Fig. 3 and Fig. 5, while the functions $h_{r_d}^\pm(\sigma)$ combine to the closed dotted curve that excludes the area around $h = 1$ and $\sigma = \pi$. Due to the stronger bound on r_d^{\min} in scenario (b) the corresponding excluded area is larger as can be seen in Fig. 5. In scenario (c) there are two possible intervals for r_d , one corresponding to the large band between the solid curves for positive ρ and one corresponding to the area between the dotted curves for negative ρ (see Fig. 7).

b. The θ_d constraint

To make use of the upper and lower bounds on θ_d in eqs. (22)–(24) we eliminate r_d from the eq. (16), getting:

$$\sin 2\theta_d = \frac{h \sin \sigma}{\sqrt{h^2 + 2h \cos \sigma + 1}} \quad \text{and} \quad \cos 2\theta_d = \frac{1 + h \cos \sigma}{\sqrt{h^2 + 2h \cos \sigma + 1}}. \quad (\text{A9})$$

Solving for h yields

$$h^\pm(\sigma, \theta_d) = \frac{\sin 2\theta_d \sin(2\theta_d \pm \sigma)}{\sin^2 \sigma - \sin^2 2\theta_d}. \quad (\text{A10})$$

In order to find the upper and lower bound on h as a function of σ from the global extrema of θ_d in eqs. (22)–(24) we have to treat carefully the discrete ambiguities of the trigonometric functions in eq. (A10). To be specific in the following we discuss the constraints in scenario (a) and (b) that arise from eq. (A3). For scenario (c) one has to consider separately the two allowed interval for θ_d due to eq. (A4). We investigate separately the following three cases:

1. $2\theta_d \in [-90^\circ, 0^\circ]$: From $2\theta_d > -32^\circ$ it follows that $\sin 2\theta_d$ increases monotonically in the interval $[-0.56, 0]$. Due to eq. (A9) the negative sign of $\sin 2\theta_d$ implies that also $\sin \sigma$ is negative and therefore $\sigma \in [180^\circ, 360^\circ]$. Taking into account that $\cos 2\theta_d \geq 0$ (and therefore $h \leq -1/\cos \sigma$ if $\sigma \in [180^\circ, 270^\circ]$) we find that there is only an upper bound on h as a function of σ :

$$h \leq h_{\theta_d}^{max}(\sigma) \equiv h^+(\sigma, \theta_d^{min}) \quad \text{for } \sigma \in [180^\circ, 360^\circ - |2\theta_d^{min}|]. \quad (\text{A11})$$

2. $2\theta_d \in [0^\circ, 180^\circ]$: In this regime there are no constraints on θ_d . Since $\text{sign}(\sin 2\theta_d) = \text{sign}(\sin \sigma)$ it follows that also for $\sigma \in [0^\circ, 180^\circ]$ we cannot derive a limit on h .
3. $2\theta_d \in [180^\circ, 270^\circ]$: From $2\theta_d < 212^\circ$ it follows that $\sin 2\theta_d$ increases monotonically in the interval $[-0.53, 0]$. Due to eq. (A9) the negative sign of $\sin 2\theta_d$ implies that also $\sin \sigma$ is negative and therefore $\sigma \in [180^\circ, 360^\circ]$. Taking into account that $\cos 2\theta_d \leq 0$ (and therefore $h \geq -1/\cos \sigma$ if $\sigma \in [270^\circ, 360^\circ]$) we find that there is only a lower bound on h :

$$h \geq h_{\theta_d}^{min}(\sigma) \equiv h^+(\sigma, \theta_d^{max}) \quad \text{for } \sigma \in [180^\circ, 2\theta_d^{max}]. \quad (\text{A12})$$

Together the constraints in eq. (A11) and eq. (A12) exclude the region between the dashed $[h_{\theta_d}^{min}(\sigma)]$ and the dashed-dotted $[h_{\theta_d}^{max}(\sigma)]$ curves in Fig. 3 and Fig. 5. For scenario (c) the analysis is similar, resulting in the dashed ($\rho > 0$) and dashed-dotted curves ($\rho < 0$) in Fig. 7.

REFERENCES

- [1] D.E. Groom *et al.*, Eur. Phys. J. **C 15**, (2000) 1.
- [2] N. Cabibbo, Phys. Rev. Lett. **10** (1963) 531;
M. Kobayashi and K. Maskawa, Prog. Th. Phys. **49** (1973) 652.
- [3] R. Forty *et al.*, ALEPH Collaboration, preprint ALEPH 99-099.
- [4] BaBar collaboration, hep-ex/0102030.
- [5] BELLE collaboration, hep-ex/0102018.
- [6] T. Affolder *et al.*, CDF Collaboration, Phys. Rev. **D 61** (2000) 072005
[hep-ex/9909003].
- [7] K. Ackerstaff *et al.*, OPAL Collaboration, Eur. Phys. J. **C 5** (1998) 379
[hep-ex/9801022].
- [8] L. Wolfenstein, Phys. Rev. Lett. **51** (1983) 1945.
- [9] *The BaBar physics book* (SLAC-R-504), Chapter 14, available at:
<http://www.slac.stanford.edu/pubs/slacreports/slac-r-504.html>.
- [10] A.J. Buras, hep-ph/0101336.
- [11] M. Ciuchini *et. al.*, hep-ph/0012308.
- [12] Y-L. Wu, Y-F. Zhou, hep-ph/0102310.
- [13] D. Atwood and A. Soni, hep-ph/0103197.
- [14] S. Plaszczynski and M.-H. Schune, hep-ph/9911280;
Y. Grossman, Y. Nir, S. Plaszczynski and M.H Schune, Nucl. Phys. **B 511** (1998) 69
[hep-ph/9709288].
- [15] G. Barenboim, G. Eyal and Y. Nir, Phys. Rev. Lett. **83** (1999) 4486 [hep-ph/9905397].
- [16] G. Eyal, Y. Nir and G. Perez, JHEP **0008** (2000) 028 [hep-ph/0008009].
- [17] Y. Nir and D. Silverman, Nucl. Phys. **B 345** (1990) 301;
C.O. Dib, D. London and Y. Nir, Int. J. Mod. Phys. **A6** (1991) 1253;
J.M. Soares and L. Wolfenstein, Phys. Rev. **D 47** (1993) 1021;
Y. Nir, Phys. Lett. **B 327** (1994) 85 [hep-ph/9402348];
Y. Grossman, Phys. Lett. **B 380** (1996) 99 [hep-ph/9603244];
N.G. Deshpande, B. Dutta and S. Oh, Phys. Rev. Lett. **77** (1996) 4499
[hep-ph/9608231];
J.P. Silva and L. Wolfenstein, Phys. Rev. **D 55** (1997) 5331 [hep-ph/9610208];

- A.G. Cohen, D.B. Kaplan, F. Lepeintre and A.E. Nelson, Phys. Rev. Lett. **78** (1997) 2300 [hep-ph/9610252];
 G. Barenboim, F.J. Botella, G.C. Branco and O. Vives, Phys. Lett. **B 422** (1998) 277 [hep-ph/9709369].
- [18] A.J. Buras, P. Gambino, M. Gorbahn, S. Jager and L. Silvestrini, Phys. Lett. **B 500** (2001) 161 [hep-ph/0007085].
- [19] A. J. Buras, P. Gambino, M. Gorbahn, S. Jager and L. Silvestrini, Nucl. Phys. **B592** (2001) 55 [hep-ph/0007313].
- [20] E. Gabrielli and G.F. Giudice, Nucl. Phys. **B 433** (1995) 3; Erratum Nucl. Phys. **B 507** (1997) 549 [hep-lat/9407029].
- [21] G. Ecker and W. Grimus, D. Chang, Nucl. Phys. **B 258** (1985) 328;
 Z. Phys. **C30** (1986) 293;
 D. Chang, Nucl. Phys. **B 214** (1983) 435.
- [22] G. Barenboim, J. Bernabeu and M. Raidal, Nucl. Phys. **B478** (1996) 527 [hep-ph/9608450].
- [23] G. Barenboim *et. al.*, Nucl. Phys. **B511** (1998) 577 [hep-ph/9611347].
- [24] G. Barenboim, J. Bernabeu and M. Raidal, Phys. Rev. **D 55** (1997) 4213 [hep-ph/9702337].
- [25] G. Barenboim, J. Bernabeu, J. Matias and M. Raidal Phys. Rev. **D60** (1999) 016003 [hep-ph/9901265].
- [26] J.M. Frere *et. al.* Phys. Rev. **D 46** (1992) 337.
- [27] P. Ball, J.M. Frere and J. Matias, Nucl. Phys. **B 572** (2000) 3 [hep-ph/9910211].
- [28] P. Ball and R. Fleischer, Phys. Lett. **B 475** (2000) 111 [hep-ph/9912319].
- [29] J.P. Silva and L. Wolfenstein, Phys. Rev. **D 55** (1997) 5331 [hep-ph/9610208];
 Y. Grossman, Y. Nir and M.P. Worah, Phys. Lett. **B 407** (1997) 307 [hep-ph/9704287];
 G. Eyal and Y. Nir, JHEP **09** (1999) 013 [hep-ph/9908296];
 G.C. Branco, P.A. Parada, T. Morozumi and M.N. Rebelo, Phys. Rev. **D 48** (1993) 1167;
 G.C. Branco, P.A. Parada, T. Morozumi and M.N. Rebelo, Nucl. Phys. Proc. Suppl. **37A** (1994) 29.
- [30] A.J. Buras and R. Buras, Phys. Lett. **B 501** (2001) 223 [hep-ph/0008273].
- [31] A.J. Buras, M.E. Lautenbacher and G. Ostermaier, Phys. Rev. **D 50** (1994) 3433

- [hep-ph/9403384].
- [32] T. Inami and C.S. Lim, *Prog. Theor. Phys.* **65** (1981) 297.
- [33] G.C. Branco, L. Lavoura and J.P. Silva, *CP Violation*, Clarendon-Oxford Press (1999) 188.
- [34] L.L. Chau and W.Y. Keung, *Phys. Rev. Lett.* **53**, (1984) 1802.
- [35] V. Fanti *et. al.*, *Phys. Lett. B* **465** (1999) 335;
T. Gershon, [hep-ph/0101034].
- [36] S. Adler *et. al.* E787 Collaboration, *Phys. Rev. Lett.* **84** (2000) 3768 [hep-ex/0002015].
- [37] ALEPH Collaboration, hep-ex/0010022.
- [38] H. Fusaoka and Y. Koide, *Phys. Rev. D* **57** (1998) 3986 [hep-ph/9712201];
M. Carena *et. al.*, hep-ph/0010338.

Tab. 1: Input values

Parameter	Value	ref.
V_{ud}	0.9735	[11]
V_{ub}	0.00355 ± 0.00036	[11]
V_{cb}	0.040 ± 0.0016	[11]
Δm_d	$(0.487 \pm 0.014) \text{ ps}^{-1}$	[11]
Δm_{B_s}	$> 15 \text{ ps}^{-1}$	[11]
$ \varepsilon_K $	0.00228	[11]
$\text{BR}(K^+ \rightarrow \pi^+ \nu \bar{\nu})$	$(1.5_{-1.2}^{+3.4}) \times 10^{-10}$	[36]
$\text{BR}(B \rightarrow X_s \nu \bar{\nu})$	$< 6.4 \cdot 10^{-4}$	[37]
η_1	1.38 ± 0.2	[11]
η_2	0.57	[11]
η_3	0.47	[11]
η_B	0.55	[10]
η_X	0.994	[10]
ξ	1.14 ± 0.05	[11]
P_c	0.31 ± 0.05	[10]
$P_0(X)$	0.42 ± 0.06	[10]
$\bar{m}_t(m_t)$	$(166 \pm 5) \text{ GeV}$	[10]
A	0.819 ± 0.040	[11]
λ	0.2237 ± 0.0033	[11]
B_K	$0.87 \pm 0.13 \text{ GeV}$	[11]
$f_{B_d} \sqrt{B_{B_d}}$	$0.23 \pm 0.025 \text{ GeV}$	[11]
κ_+	4.11×10^{-11}	[10]

Tab. 2: Input values for the SBLR model

Parameter	Value	ref.
$\bar{m}_u(M_Z)$	0.0023 ± 0.00042 GeV	[38]
$\bar{m}_d(M_Z)$	0.0047 ± 0.0006 GeV	[38]
$\bar{m}_c(M_Z)$	0.677 ± 0.056 GeV	[38]
$\bar{m}_s(M_Z)$	0.0934 ± 0.012 GeV	[38]
$\bar{m}_t(M_Z)$	181 ± 13 GeV	[38]
$\bar{m}_b(M_Z)$	3 ± 0.11 GeV	[38]
M_{W_2}	8000 ± 5000 GeV	[27]
M_H	12000 ± 2000 GeV	[27]
δ_K	0.35 ± 0.1	[22]
$B_B^S(m_b)/B_B(m_b)$	1.2 ± 0.2	[27]
t_1	0.231	-
t_2	0.041 ± 0.018	-
t_3	0.016 ± 0.0016	-
η_4	5 ± 1.5	[22]

FIGURES

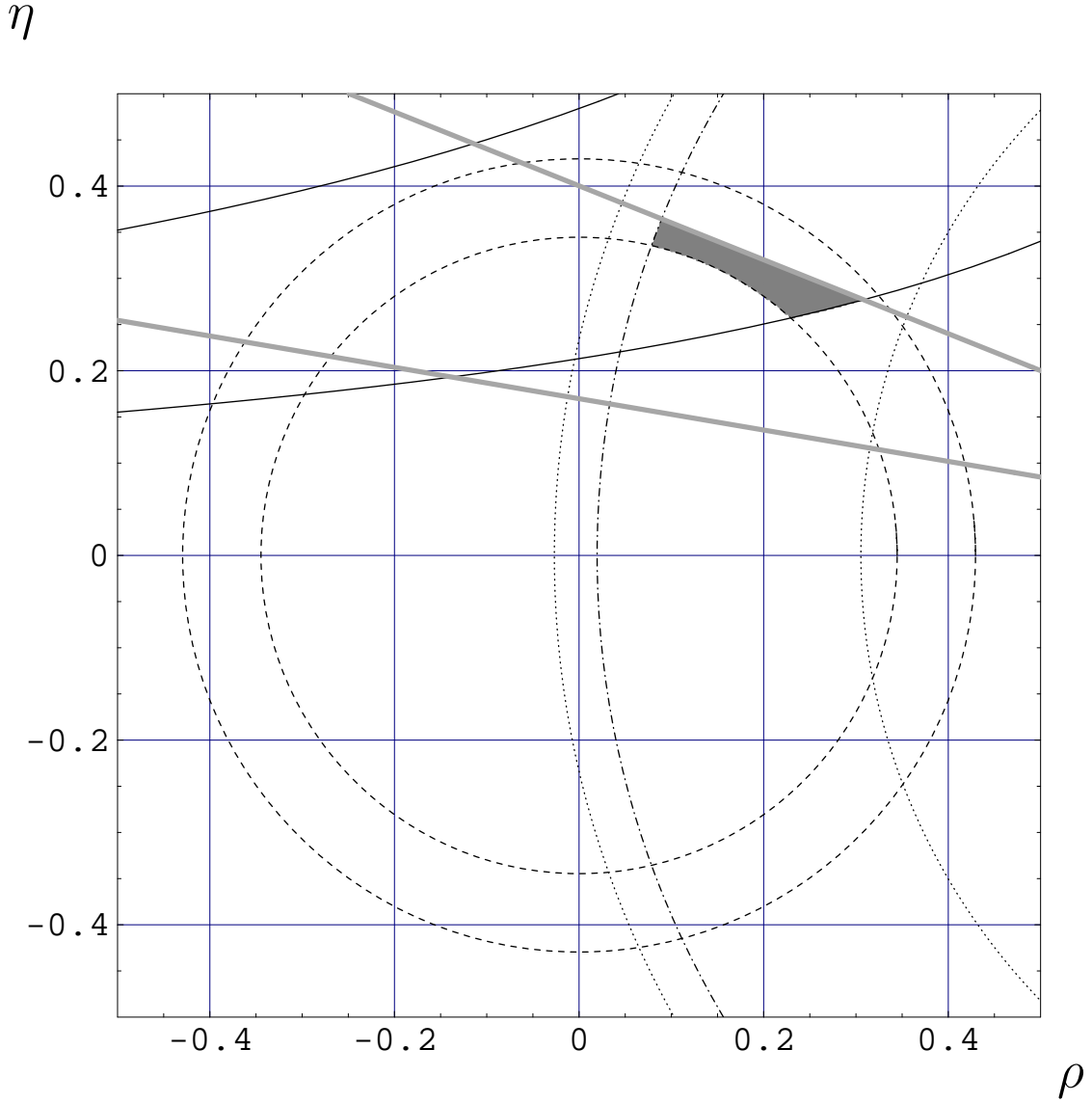


FIG. 1. Determination of the apex (ρ, η) of the unitarity triangle: The grey area is the presently allowed region, which is determined by (a) the measurement of $|V_{ub}/V_{cb}|$ (dashed circles), (b) the observed $B_d^0 - \bar{B}_d^0$ mixing parameter Δm_d (dotted circles), (c) the lower bound on the $B_s^0 - \bar{B}_s^0$ mixing parameter Δm_s (dashed-dotted circle), (d) the measurement of ε_K (solid hyperbolae) and (e) the combined result of the CDF, BELLE and BaBar measurements of $a_{\psi K_S}$ (thick grey lines).

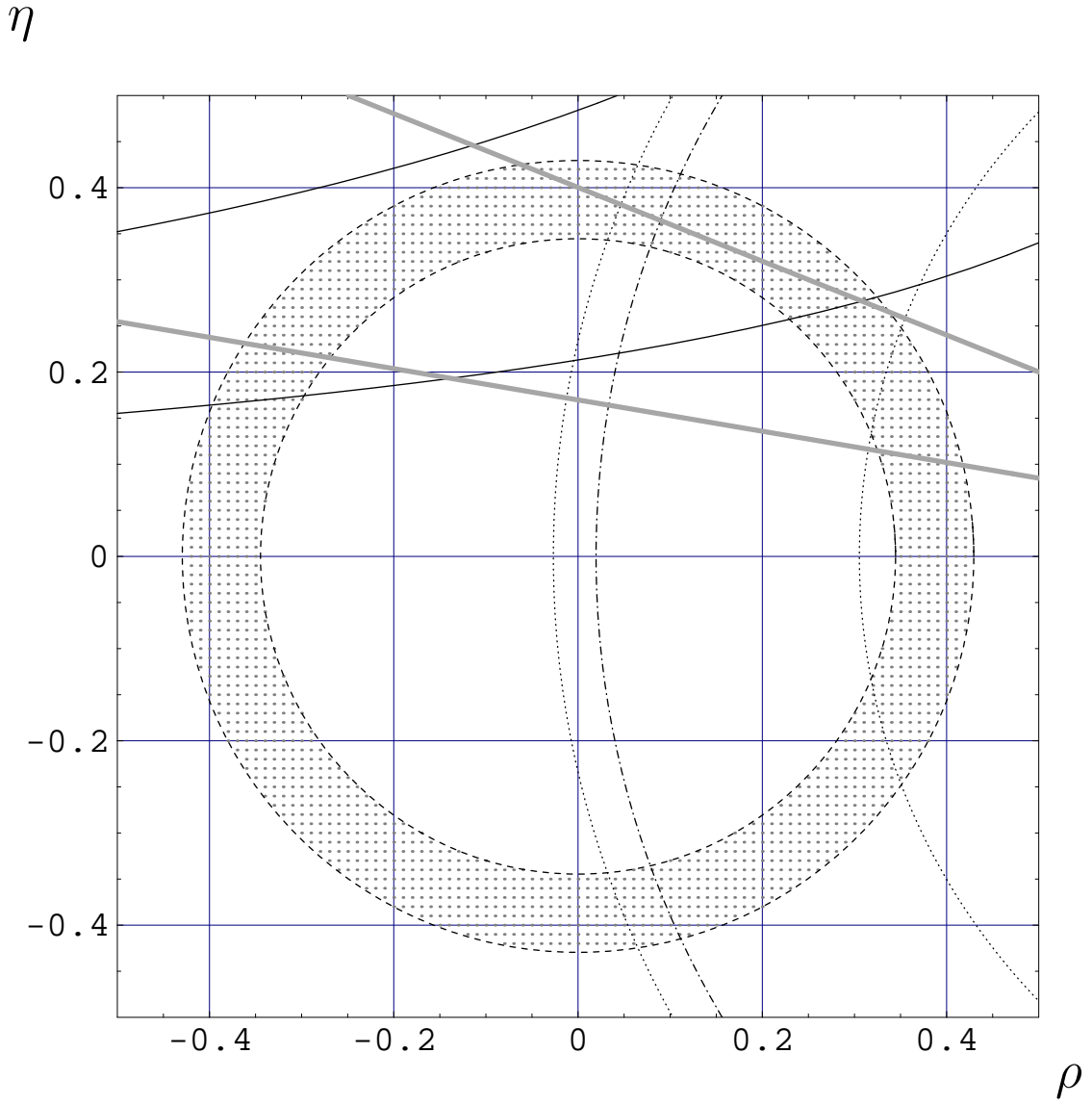


FIG. 2. The shaded area corresponds to the allowed region in the $\rho - \eta$ plane for scenario (a). It is constrained solely by $R_u \in [0.34, 0.43]$, which is determined by the measurement of $|V_{ub}/V_{cb}|$ (dashed circles). For comparison we also show the other constraints appearing in Fig. 1, which are not relevant here.

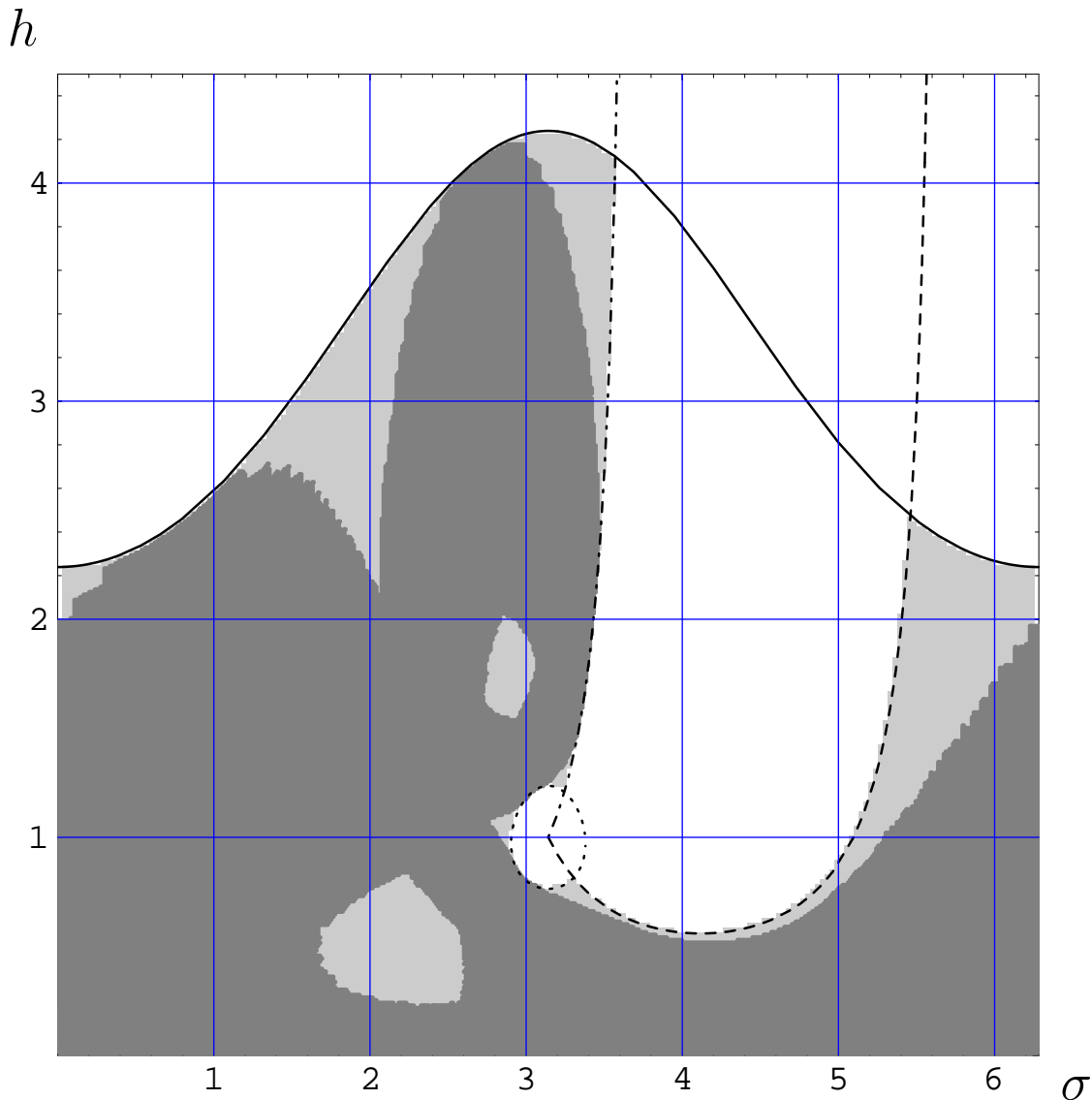


FIG. 3. The dark area corresponds to the allowed region in the $h - \sigma$ plane for scenario (a) according to our numerical analysis. It is embedded in the light area that results from the analytical boundaries based on the global constraints on r_d from $\Delta m_{d,s}$ and θ_d from $a_{\psi K_S}$. Specifically the allowed range of r_d excludes h to be above $h_{r_d}^{max}(\sigma)$ (solid curve) or between $h_{r_d}^{\pm}(\sigma)$ (dotted curves), while the allowed range of θ_d exclude the region between $h_{\theta_d}^{min}(\sigma)$ (dashed curve) and $h_{\theta_d}^{max}(\sigma)$ (dashed-dotted curve). The numerical results are not much more constraining than the analytical ones, except for the “holes” in the dark regions that correspond to the excluded region within the R_u annulus, which has been ignored in “global” analysis. (See appendix A 2 for details.)

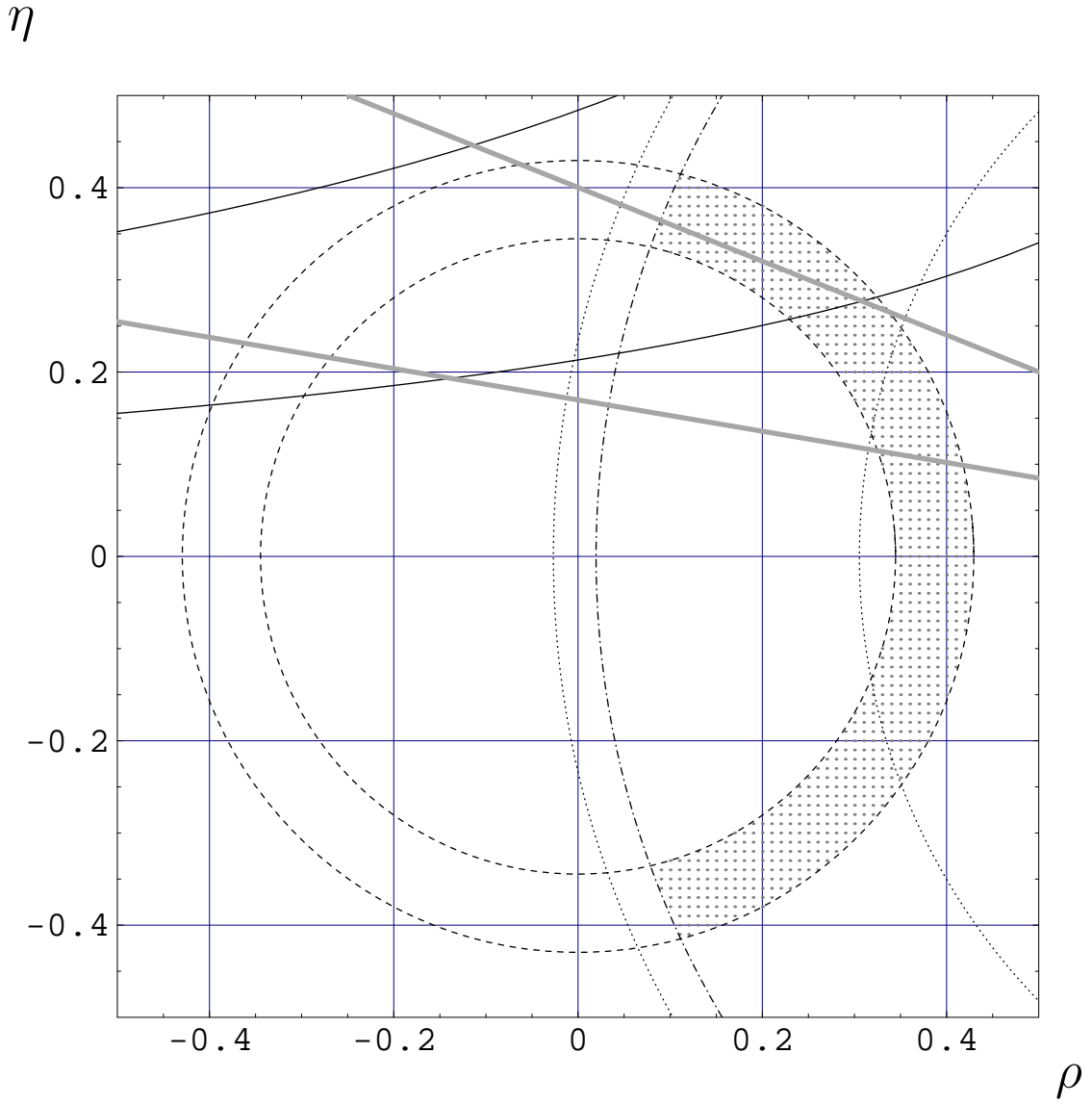


FIG. 4. The shaded area corresponds to the allowed region in the ρ – η plane for scenario (b). It is constrained by $R_u \in [0.34, 0.43]$ (dashed circles) and $\Delta m_s/\Delta m_b$ (dashed-dotted circle). For comparison we also show the other constraints appearing in Fig. 1, which are not relevant here.

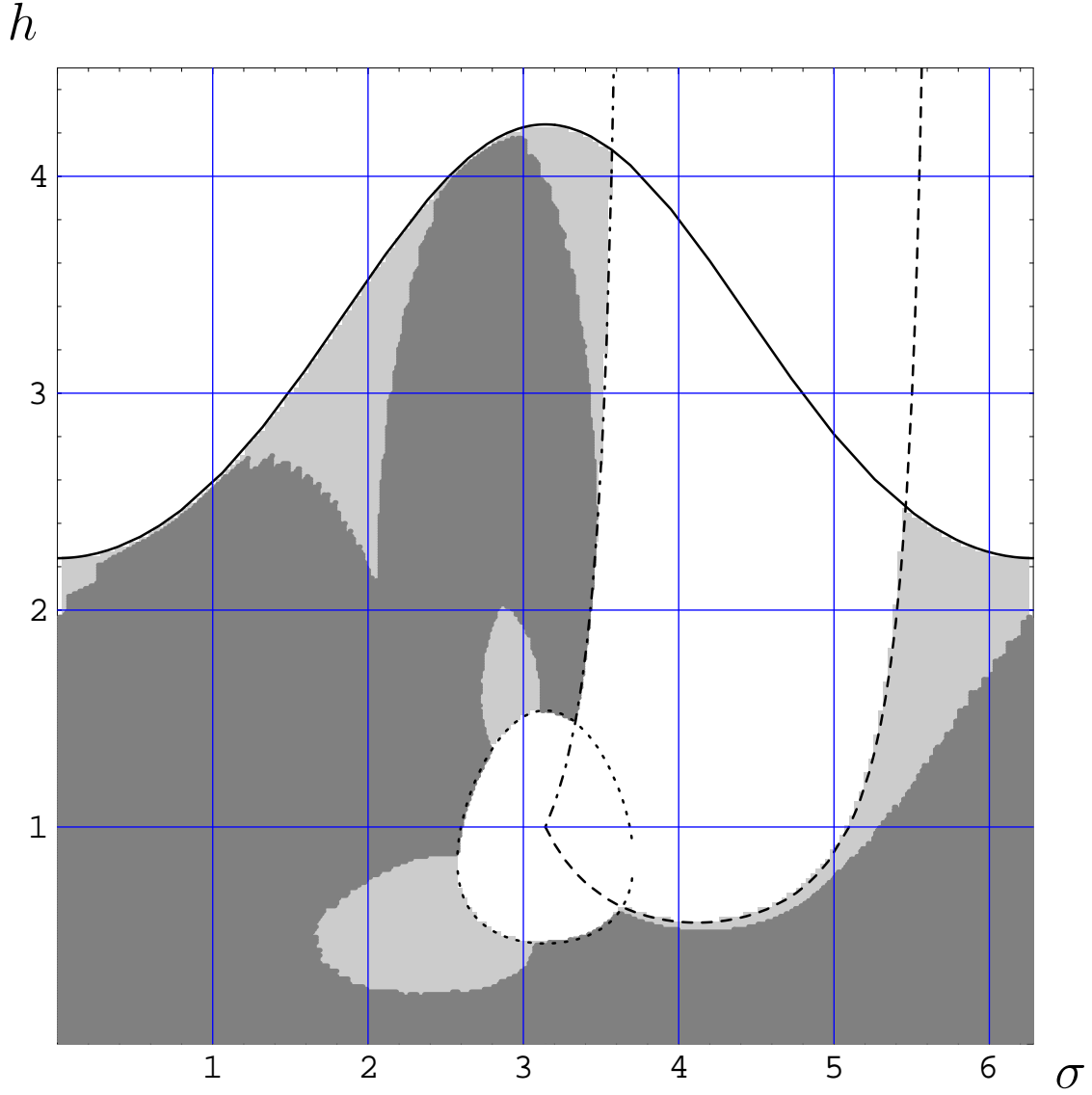


FIG. 5. The dark area corresponds to the allowed region in the $h - \sigma$ plane for scenario (b) according to our numerical analysis. It is embedded in the light area that results from the analytical boundaries based on the global constraints on r_d from $\Delta m_{d,s}$ and θ_d from $a_{\psi K_S}$. Specifically the allowed range of r_d excludes h to be above $h_{r_d}^{max}(\sigma)$ (solid curve) or between $h_{r_d}^{\pm}(\sigma)$ (dotted curves), while the allowed range of θ_d excludes the region between $h_{\theta_d}^{min}(\sigma)$ (dashed curve) and $h_{\theta_d}^{max}(\sigma)$ (dashed-dotted curve). Due to the stronger bound on r_d^{min} in scenario (b) the excluded area from $h_{r_d}^{\pm}(\sigma)$ is larger than in Fig. 3. (See appendix A 2 for details.)

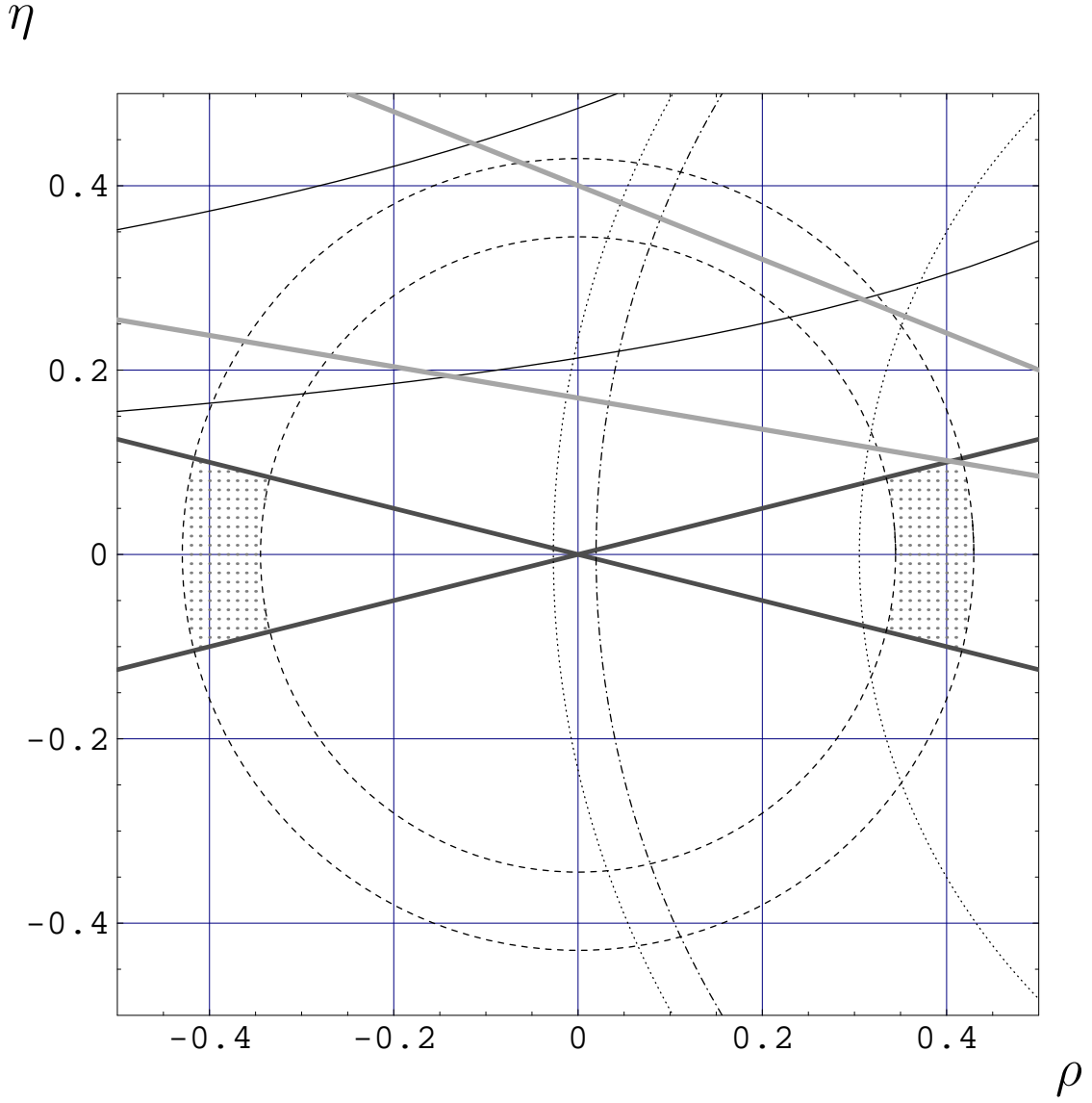


FIG. 6. The shaded area corresponds to the allowed region in the $\rho - \eta$ plane for scenario (c). It is constrained by $R_u \in [0.34, 0.43]$ (dashed circles) and $\tan \delta_{KM} < 0.25$ (“small phase”). For comparison we also show the other constraints appearing in Fig. 1, which are not relevant here.

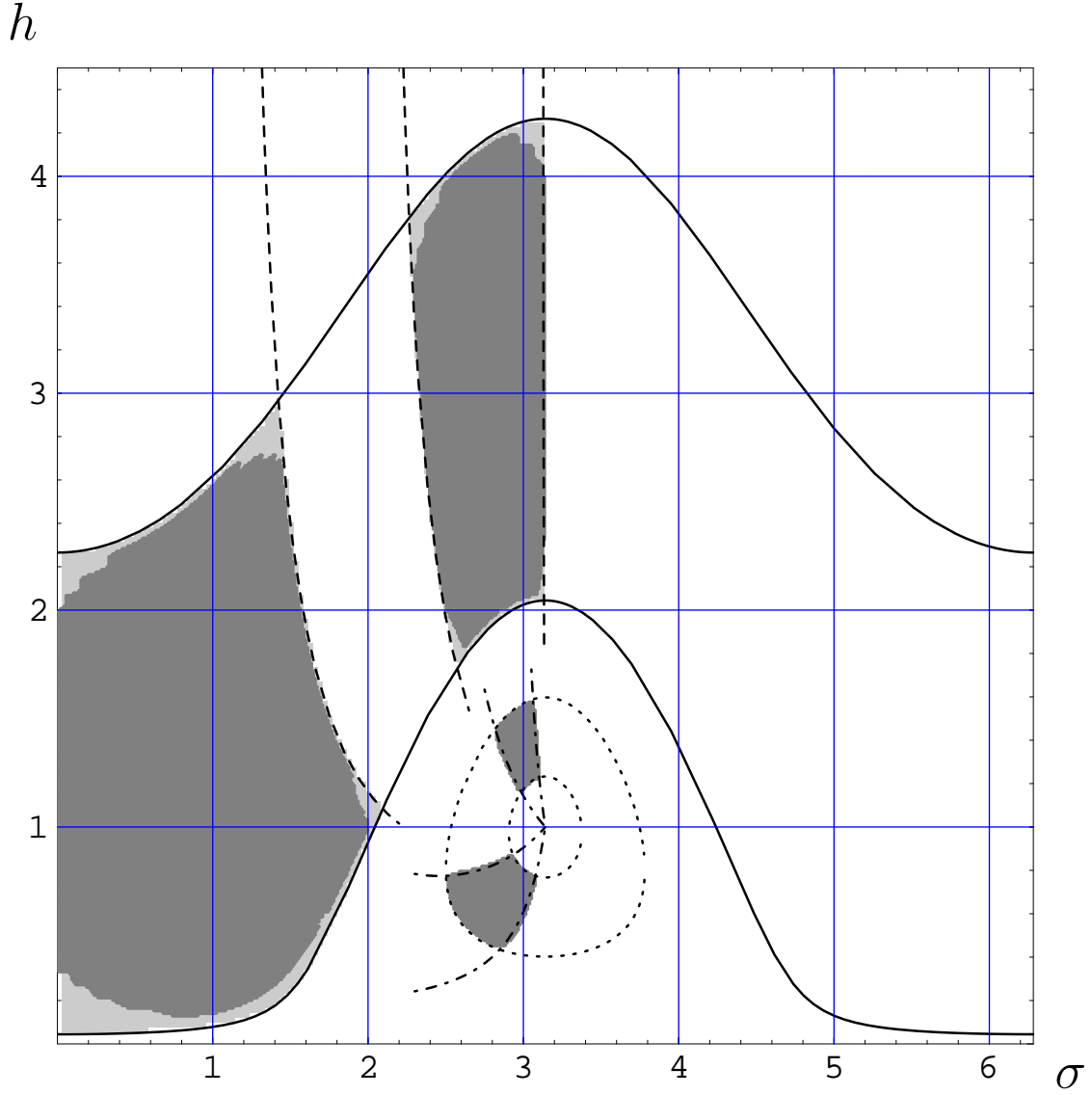


FIG. 7. The dark area corresponds to the allowed region in the $h - \sigma$ plane for scenario (c) according to our numerical analysis. It is embedded in the light area that results from the analytical boundaries based on the global constraints on r_d from $\Delta m_{d,s}$ and θ_d from $a_{\psi K_S}$. Specifically there are two possible intervals for r_d , one corresponding to the large band between the solid curves for positive ρ and one corresponding to the area between the dotted curves for negative ρ . The allowed ranges of θ_d limit the allowed region to be between the dashed ($\rho > 0$) and dashed-dotted curves ($\rho < 0$). Note that unlike for scenarios (a) and (b) in scenario (c) h has a lower bound and σ has an upper bound. (See appendix A 2 for details.)

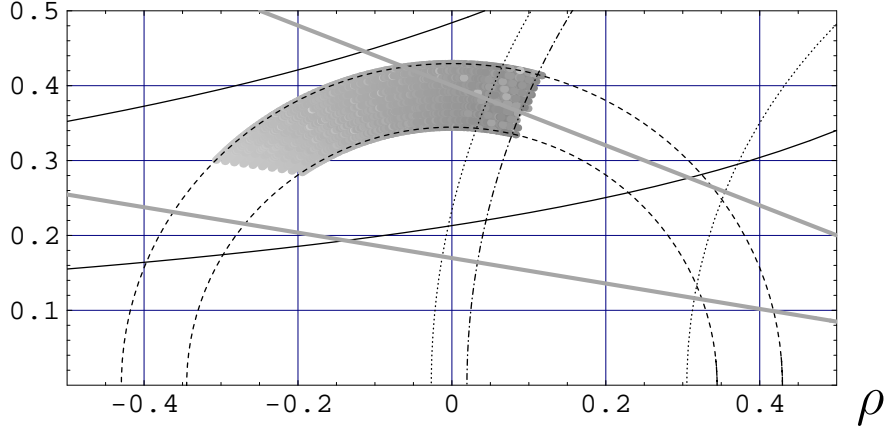
η 

FIG. 8. The shaded area corresponds to the “first” solution resulting from eqs. (4), (30) and (31) within models of MFV. The grey scale indicates the magnitude of F_{tt} as a function of ρ and η : The lightest region corresponds to $F_{tt} \simeq 0.4$ and the darkest region corresponds to $F_{tt} \simeq 2.7$. Adding the constraint from $\Delta m_s/\Delta m_b$ (dashed-dotted circle) practically the entire solution presented in this figure is excluded.

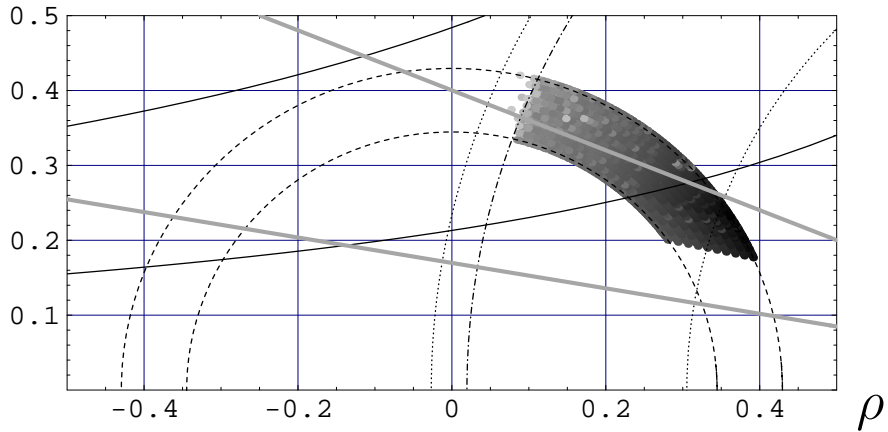
 η 

FIG. 9. The shaded area corresponds to the allowed region according to the “second” solution resulting from eqs. (4), (30) and (31) within models of MFV. The grey scale indicates the magnitude of F_{tt} as a function of ρ and η : The lightest region corresponds to $F_{tt} \simeq 1.2$ and the darkest region corresponds to $F_{tt} \simeq 5.7$.